Guided transition waves in multistable mechanical metamaterials

Lishuai Jin[a,b,1], Romik Khajehtourian[c,1], Jochen Mueller[a,d,1], Ahmad Rafsanjani[a,e,1], Vincent Tournat[f], Katia Bertoldi[a,d,g,2], and Dennis M. Kochmann[c,h,2]

[a]John A. Paulson School of Engineering and Applied Sciences, Harvard University, Cambridge, MA 02138; [b]Department of Mechanics, Tianjin University, Tianjin 300072, China; [c]Department of Mechanical and Process Engineering, ETH Zürich, 8092 Zürich, Switzerland; [d]Wyss Institute for Biologically Inspired Engineering, Cambridge, MA 02138; [e]Department of Materials, ETH Zürich, 8093 Zürich, Switzerland; [f]Laboratoire d'Acoustique de l'Université du Mans, CNRS UMR 6613, Le Mans Université, 72085 Le Mans, France; [g]Kavli Institute, Harvard University, Cambridge, MA 02138; and [h]Graduate Aerospace Laboratories, California Institute of Technology, Pasadena, CA 91125

Edited by Huajian Gao, Nanyang Technological University, Singapore, and approved December 27, 2019 (received for review August 1, 2019)

Transition fronts, moving through solids and fluids in the form of propagating domain or phase boundaries, have recently been mimicked at the structural level in bistable architectures. What has been limited to simple one-dimensional (1D) examples is here cast into a blueprint for higher dimensions, demonstrated through 2D experiments and described by a continuum mechanical model that draws inspiration from phase transition theory in crystalline solids. Unlike materials, the presented structural analogs admit precise control of the transition wave's direction, shape, and velocity through spatially tailoring the underlying periodic network architecture (locally varying the shape or stiffness of the fundamental building blocks, and exploiting interactions of transition fronts with lattice defects such as point defects and free surfaces). The outcome is a predictable and programmable strongly nonlinear metamaterial motion with potential for, for example, propulsion in soft robotics, morphing surfaces, reconfigurable devices, mechanical logic, and controlled energy absorption.

mechanical metamaterial | multistability | structure | phase transformation | nonlinear dynamics

Mechanical metamaterials have been riding on a (transition) wave in recent decades, transforming the way in which we think of material behavior—no longer as nature-given but rather as tailorable for enhanced performance and functionality in everyday applications (1–3). Testament to this development is the now well-established phononic and acoustic metamaterials to control mechanical waves in unprecedented ways (4) and to facilitate applications such as nonreciprocal transmission (5, 6), cloaking (7), and noise reduction (8–10). Common to all these systems is that they operate in the linear regime and take advantage of spectral gaps in frequency (11), possibly tailorable by finite predeformation such as in bistable systems (12, 13). By contrast, nonlinear dynamic counterparts are still rare, even though they have shown tremendous potential for controlling mechanical signals (14–17) and unraveling unique effects such as unidirectional wave motion (18). The most prominent cause of nonlinearity in those examples is a nonconvex, multiwelled energy landscape, which was shown to support the stable propagation of topological defects (19).

Natural materials systems are rich in propagating transition fronts that separate distinct phases (or domains) through phase (or domain) boundaries. Examples range from temperature- and stress-induced solid–solid phase transformations in crystalline materials (20, 21); to domain wall motion in ferroelectrics, ferromagnetics, and multiferroics (22–24); to deformation twinning in metals and ceramics (25). In each case, a nonconvex potential energy landscape is responsible for the existence of multiple stable equilibrium states (e.g., multiple phases or domains), and the application of external stimuli drives transition fronts between domains. The multiwelled energy landscape renders the resulting system kinetics inherently nonlinear and the associated transition phenomena complex to describe (26, 27) and to imitate in artificial systems. Demonstrated structural analogs so far have been limited to one-dimensional (1D) periodic chains (15, 18); extensions to 2D configurations have been limited to numerical studies of grounded systems with each unit cell attached to a bistable on-site potential (28)—making the resulting architectures immobile and of limited applicability.

In this work, we use a combination of analysis and experiments to demonstrate transition waves in a class of 2D architectures previously employed only for static reconfiguration. Specifically, we focus on monostable unit cells which, when tessellated, form an untethered and ungrounded network in which each unit cell displays multistability. The transition from monostability to bistability emerges from the suppression of rotational rigid-body modes of individual unit cells by the enforcement of periodicity in tessellated networks. We leverage a continuum mechanical model of solid–solid phase transitions to qualitatively and quantitatively describe the observed dynamic effects and to aid in the design process. Then, guided by simulations, we experimentally demonstrate the steering of transition fronts

Significance

Mimicking material-level phenomena using macroscopically architected materials has gained popularity and enabled novel engineering applications such as photonic, acoustic, mechanical, and topological metamaterials. An interesting microstructural phenomenon observed in phase-transforming materials is the dissipative motion of topological defects such as phase and domain boundaries. With a few one-dimensional exceptions, structural analogs of dynamic phase-transforming materials are still rare, owing to their complicating strong nonlinearity. Through experiments, models, and simulations, we demonstrate a concept for tailoring propagating transition fronts in periodic structures in arbitrary dimensions. This significantly increases the design space of metamaterial performance and functionality and finds application in programming soft robotic locomotion, in controlling energy absorption (or release), and in mechanical logic devices.

Author contributions: K.B. and D.M.K. designed research; L.J., R.K., J.M., A.R., V.T., and D.M.K. performed research; R.K. contributed new reagents/analytic tools; L.J., R.K., J.M., A.R., and D.M.K. analyzed data; and K.B. and D.M.K. wrote the paper.

The authors declare no competing interest.

This article is a PNAS Direct Submission.

Data deposition: All simulation data, scripts, and experimental data are available on Figshare, https://doi.org/10.6084/m9.figshare.10048724.v2.

[1]L.J., R.K., J.M., and A.R. contributed equally to this work.

[2]To whom correspondence may be addressed. Email: dmk@ethz.ch or bertoldi@seas.harvard.edu.

This article contains supporting information online at https://www.pnas.org/lookup/suppl/doi:10.1073/pnas.1913228117/-/DCSupplemental.

through carefully engineered topological defects (akin to point defects and free surfaces in crystal lattices; Fig. 1). This leads to morphing and reconfigurable structures with not only tailored initial and final configurations but the entire kinetic transformation path—including the wave travel direction, trajectory, and velocity—geared toward a time-dependent deployment history with programmable intermediate states. Besides enabling opportunities for actuated all-soft, substrate-free engineering applications from soft robotics to "4D printing" (29–31), our work also highlights avenues to replicate rich material-level kinetic phenomena at the structural level.

Multistable Structural Networks

The point of departure is a structural network whose unit cells, once periodically connected, experience two stable configurations: the unstrained ground state and a strained (here, volumetrically expanded) equilibrium state of higher strain energy (Fig. 2). This setup is akin to solid–solid phase transitions and represents our starting point for guiding transition fronts. Multistability is key to achieving topological domain boundaries in the structural network between open (strained) and closed (unstrained) unit cells. The high level of elastic strain energy in partially open or closed unit cells favors the formation of large domains of uniform equilibrium strain, separated by domain boundaries of generally diffuse character and accommodated by transitioning unit cells of high energy (collectively contributing interface energy). Stable static configurations of the structural network are hence minima of its total energy, subject to particular boundary conditions. Upon changes to the loading, domain boundaries move, and transition fronts propagate (Fig. 1 and Movie S1).

As shown in Fig. 2 *A* and *B*, the unit cell is based on four triangular building blocks containing slender joints that admit large reversible local rotations, producing auxetic expansion upon loading (32, 33), and pins that stiffen the unit cell in compression (*SI Appendix*, Fig. S3). Its geometry is defined by the dimensionless ratios l/L, δ/L, and a/L, where l, δ, a, and L denote, respectively, the hinge length, hinge thickness, core length, and unit cell size. While variation in these parameters enables control of the energy landscape (33), our experimental prototypes in this study are characterized by $l/L = 0.15$, $\delta/L = 0.02$, and $a/L = 0.3$ (with $L = 27$ mm). We find that such unit cells are monostable if free-standing but bistable when tessellated (*SI Appendix*, Figs. S6 and S7). More specifically, while a free-standing unit cell exhibits a single equilibrium in the undeformed ground state (Fig. 2*D*), our simulations indicate a bistable behavior for the 3×3 tessellation, as the load vanishes in the expanded state at an applied displacement of *ca*. 22 mm (Fig. 2*E* and *SI Appendix*, Figs. S4–S6; note that experiments record a small positive force in that state, which is attributed to friction in the clamps and the resolution of the load cell). Therefore, as in classical phase transitions (34), the overall sample size of our multistable metamaterials and the particular boundary conditions have an essential impact on the (multi)stability of the network (here demonstrated by the influence of the number of columns and rows per sample; *SI Appendix*, Fig. S8).

Finally, in addition to free surfaces, the introduction of zeroth-order lattice defects in the form of isolated point defects (modified unit cells) affects the stability as well as the domain nucleation and the domain wall migration within samples (Fig. 2)—the latter being reminiscent of Zener drag on domain walls by point defects (35). As shown in Fig. 1, all such architectural features can be exploited to guide transition fronts of complex shapes and paths.

Continuum Mechanical Model

Having demonstrated the fundamental concept of transition fronts in multistable structural networks (Fig. 1), we introduce a continuum model to describe and efficiently simulate the domain formation and growth processes. The model will be used for the exploration of the design space of 1D, 2D, and 3D transition waves with and without defects.

Leveraging the analogy to solid–solid phase transitions (20, 36, 37), we borrow from continuum mechanics to describe the observed domain kinetics by a simple analytical model, based on the observations that 1) each unit cell has two

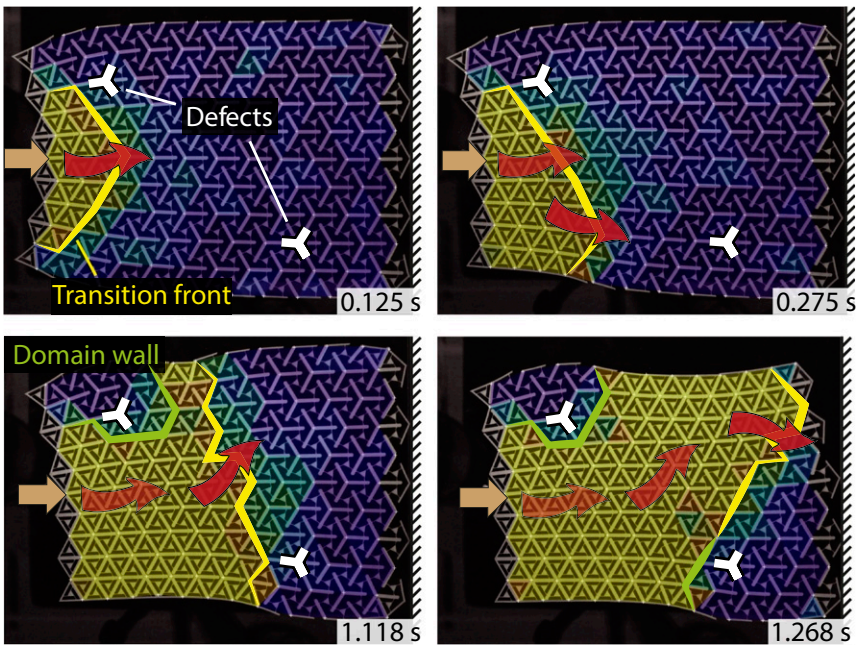

Fig. 1. Upon initiation by an impulse (orange arrow), a transition front propagates through a 2D periodic multistable network, transforming unit cells from an open (strained) to a closed (unstrained) state as the domain wall passes by. Lattice defects and boundaries can be used effectively to predicatively guide the wave in the laser-cut polymer sheet (the right boundary acts as a rigid wall here).

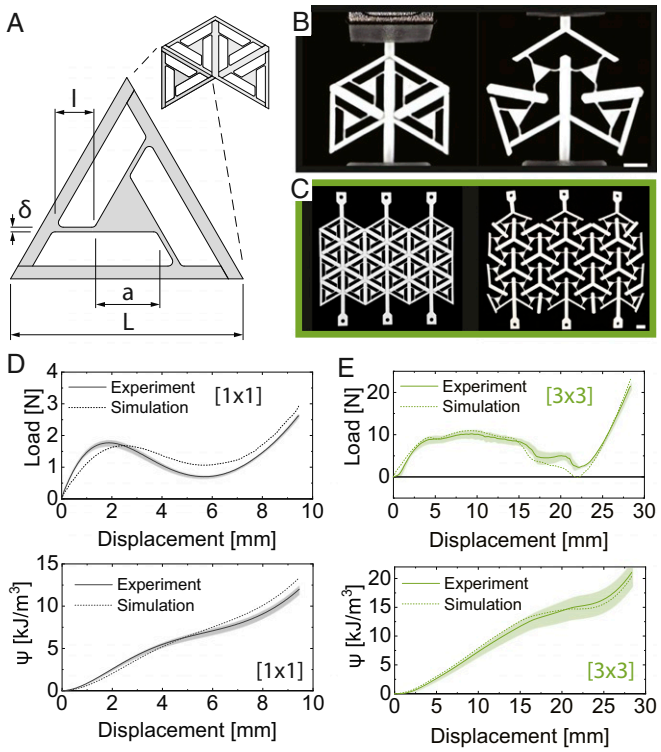

Fig. 2. Unit cell geometry, tessellation, and response. (*A*) Geometric parameters defining the unit cell, which consists of four triangular building blocks (material is gray, voids are white). (*B*) Snapshots of an individual unit cell in the undeformed configuration and loaded by an applied displacement of 9.45 mm. Note that, since a single unit cell is monostable, the structure returns to the undeformed configuration as soon as the clamps used to stretch the structure are removed. (*C*) Snapshots of a 3×3 unit cell tessellation in the undeformed configuration and in the stable expanded configuration. Since the tessellation is multistable, it remains in the expanded state when the clamps used to stretch it are removed. (Scale bars for *B* and *C*, 10 mm.) (*D* and *E*) Load–displacement curves and associated potential energy densities ψ (defined by first fitting a fifth-degree polynomial to the measured force–displacement data and then integrating) for (*D*) a single unit cell and (*E*) a 3×3 tessellation. Both experimental (continuous line) and finite element results are shown.

energy-minimizing strain states, 2) inertial effects of the thin structure and ground friction play a negligible role, and 3) the lossy base material leads to viscous dissipation during deformation. As in classical homogenization, we consider a separation of scales between the unit cell size L and the overall sample dimensions, so that the sample deformation can be described by a continuous displacement field $\boldsymbol{u}(\boldsymbol{x}, t)$ at a location $\boldsymbol{x}$ at time t. Assuming linearized kinematics, the strain tensor follows as $\boldsymbol{\varepsilon} = \mathrm{sym}(\nabla \boldsymbol{u})$. Acknowledging that the bistability is linked to volumetric straining (in d dimensions), we decompose the strains into the scalar volumetric strain $\theta = \mathrm{tr}\,\boldsymbol{\varepsilon}/d$ and the deviatoric (volume-preserving) strain tensor $\boldsymbol{e} = \boldsymbol{\varepsilon} - \theta \boldsymbol{I}$. Based on this kinematic description and the above constitutive observations, we postulate an isotropic elastic energy density $W(\boldsymbol{\varepsilon}) = \psi(\theta) + \mu\, \boldsymbol{\varepsilon} \cdot \boldsymbol{\varepsilon}$, where $\psi(\cdot)$ denotes the bistable energy landscape identified from the volumetric straining of the unit cell (*SI Appendix*, Fig. S9), and $\mu > 0$ acts as an effective shear modulus penalizing strain variations between unit cells (hence contributing energy in the interfaces between domains). ψ is chosen as a quartic polynomial to approximate the bistable energy obtained from finite element analysis (FEA) and calibrated by experiments, whereas μ is identified by homogenization of the discrete unit cell energy (*SI Appendix*, section 3).

Following the Coleman–Noll procedure of continuum mechanics, this energy density defines the elastic stress tensor as $\boldsymbol{\sigma}_e = \partial W / \partial \boldsymbol{\varepsilon}$. To account for material-intrinsic damping, we decompose the total stress tensor into elastic and viscous contributions, that is,

$$\boldsymbol{\sigma} = \boldsymbol{\sigma}_e + \boldsymbol{\sigma}_v = \frac{\partial W}{\partial \boldsymbol{\varepsilon}} + \eta\, \dot{\boldsymbol{\varepsilon}} = \eta\, \dot{\boldsymbol{\varepsilon}} + \frac{\psi'(\theta)}{d} \boldsymbol{I} + \mu\, \boldsymbol{e}, \qquad [1]$$

where $\eta > 0$ represents a Newtonian viscosity, and dots denote partial derivatives with respect to time. The point-wise equation of motion for the mechanical system, linear momentum balance in the absence of inertial effects and body forces (gravity acting perpendicular to the plane), becomes

$$\nabla \cdot \boldsymbol{\sigma} = 0 \quad \Leftrightarrow \quad \eta\, \nabla \cdot \dot{\boldsymbol{\varepsilon}} + \frac{\psi''(\theta)}{d^2} \nabla \theta + \mu\, \nabla \cdot \boldsymbol{e} = 0. \qquad [2]$$

When discreteness effects can be neglected, Eq. **2** describes the mechanics of the multistable network at the continuum level (in principle, in arbitrary dimensions d), which is solved numerically for the displacement field $\boldsymbol{u}(\boldsymbol{x}, t)$, using a finite element spatial discretization and implicit time integration. Simulations start from a fully stretched equilibrium configuration and predict the time evolution upon applied loading—leading to a transition wave that reconfigures the structure into its collapsed equilibrium state. The only calibration parameter, η, is chosen by direct comparison of transition wave speeds obtained from this continuum model and experiments of uniaxial (1D) transition waves (Fig. 3).

Uniaxial Transition Waves

Long and slender chains comprising 32×2 unit cells are initialized in their stretched equilibrium state (Fig. 3*A*) and compressed by a gradually increasing indenter force until a transition wave is triggered and subsequently propagates through the chain (Movie S2). The experimental snapshots in Fig. 3*E* confirm that a phase boundary propagates through the 1D body, gradually transforming unit cells from the open (high-energy) to the closed (low-energy) equilibrium state. To quantify this transition, we use the relative change in area,

$$\Delta A = \left| \frac{A}{A_0} \right|, \qquad [3]$$

as a continuous metric for phase identification (with A and A_0 denoting the measured current and initial unit cell size, respectively). The average wave speed measures 5.2 m/s, requiring 0.166 s to traverse the entire chain (a constant speed is reached within the first unit cell, after the decay of transient effects due to the initiation). Interestingly, defective unit cells (as seen, e.g., in the upper boundary region of Fig. 3*A*) show a vanishing impact on the propagating transition wave, demonstrating the robustness of the system against fabrication-induced imperfections.

Importantly, results obtained from describing the 1D chain dynamics by the above continuum model (Fig. 3 *G* and *H*) reveal convincing agreement with experiments, for example, comparing the measured and simulated wave profiles at time stamps 0.036, 0.094, 0.134, and at 0.166 s, confirming the applicability of the chosen linear kinetics and of the continuum description (Movie S2). Simulations yield a constant wave speed (and hence constant slope in the x–t diagram, Fig. 3*H*) after the decay of transient effects, while disturbances in experimental data (Fig. 3*G*) are attributed to fabrication imperfections and unavoidable frictional losses. It is remarkable that the wave speed shows little dependence of the triggering impulse (as long as it is sufficient to induce the transition front). Similar to grounded 1D

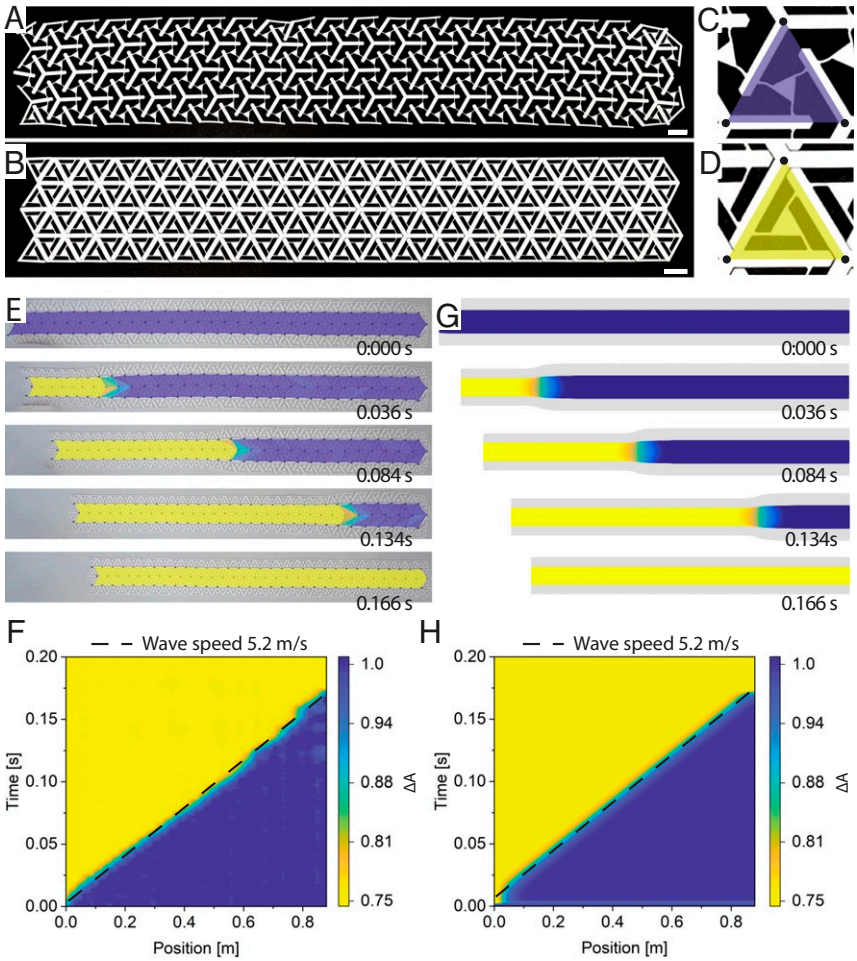

Fig. 3. The 1D transition waves. (*A* and *B*) Tessellations of bistable unit cells in their (*A*) open and (*B*) closed equilibrium states. (Scale bars, 20 mm.) (*C* and *D*) A color map shows the relative change in unit cell area, here indicating closed as blue and open as yellow. (*E*) Upon initiation from the left, a 1D transition wave travels through the structure, whose (*F*) *x*–*t* diagram confirms the approximately constant wave speed. (*G*) The transition front motion is reproduced by the continuum model in agreement with the experiment, also seen in (*H*) the *x*–*t* diagram.

chains (19), the constant speed is the result of a balance between energy release from transforming unit cells, on the one hand, and energy consumption due to viscous losses and kinetic energy of the growing tail end of the chain undergoing rigid-body motion, on the other hand (the latter being of minor importance here due to negligible inertial effects).

Controlling Transition Waves by Defects in Two Dimensions

Assembling unit cells into multistable 2D structures adds more than an additional dimension: Analogous to domain wall interactions with lattice defects in crystalline solids, the introduction of point and line defects in two dimensions provides opportunities for complex transition front guidance (*SI Appendix*, Fig. S10). Contrary to topological defects utilized to facilitate localized soft modes in a structure (38, 39), we here introduce stiff defects (akin to, e.g., precipitates or solute atoms in a crystal) that locally interact with—and thereby pin or redirect—the propagating transition front (see *SI Appendix*, Fig. S10 for details of the induced defects). Similarly, boundaries (such as stress-free surfaces; *SI Appendix*, Figs. S11 and S12) interact with the transition front and locally alter the propagation speed, thus affecting the front profile and shape.

Fig. 4 illustrates five examples of propagating transition fronts (comparing experiments and simulations for each; Movie S3), demonstrating the influence of defects and boundary conditions on the path of the transition wave. When the 2D body is indented symmetrically by a point load (Fig. 4*A*, row 1), a 1D front propagates, here showing edge effects that arise from the free boundaries and producing a convex shaped front. By contrast, when initiating the wave asymmetrically, for example, by an eccentric point load (Fig. 4*A*, row 2), a wave is generated in the transverse direction with a concave front, ultimately propagating orthogonally to the direction of initiation.

Stiff point defects (namely, open unit cells of the same size but constrained to not collapse under load) interact with propagating transition fronts by local pinning in the bulk of the structure. For example, when adding a defect at the center of a symmetric structure, the transition front is locally deflected and travels around the defect (Fig. 4*A*, row 4). If the sample is sufficiently small (Fig. 4*A*, row 3), the front may also be fully arrested due to the large driving force required to unpin the wave [akin to, e.g., the inverse scaling of the strength of Zener pinning (35) with the distance between two defects]. Deliberately tailoring defect locations, in combination with free boundaries, can hence be exploited to guide transition fronts in a complex fashion. Repeating, for example, the scenario of Fig. 4*A*, row 2, but with a point defect in the bottom right corner, results in a transition front that propagates around the defect (Fig. 4*A*, row 5).

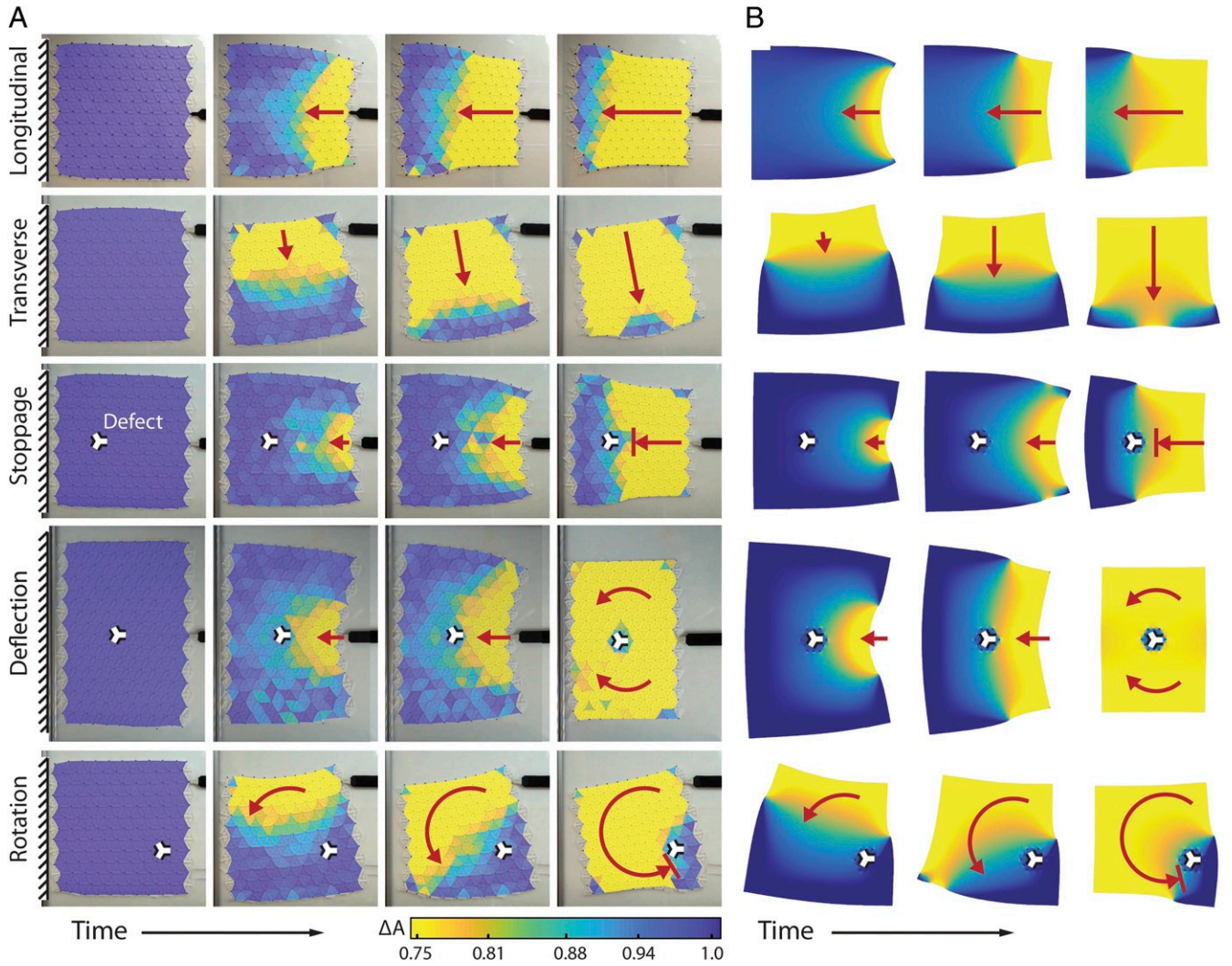

Fig. 4. The 2D transition waves. (*A*) Experimental observations of transition waves propagating through 2D structures (after initialization in the fully open configuration, each transition wave is triggered by a point load applied by the black indenter). Waves are controlled by boundary conditions (e.g., boundary application sites) as well as by defects (e.g., point defects realized by nontransforming open unit cells). Examples show free transition wave propagation in two directions, wave pinning, wave deflection, and rotation. (*B*) Numerical results obtained from the continuum model are in good agreement with experimental findings (differences stemming mainly from imperfections and size effects).

Fig. 4*B* summarizes analogous simulation results for those five cases and demonstrates the power of the continuum model toward predicting transition fronts. Of course, differences between experiments and simulations are expected due to, for example, fabrication imperfections, imperfect boundary conditions, and size effects. Considering the relatively small size of samples and the large ratio of unit cell to sample size (whereas the model assumes a separation of scales), it is remarkable that the simple model captures the qualitative transition front behavior well—thus offering predictive support in the design of tailored configurations for guided transition fronts.

Expansion of the Design Space

Having demonstrated the general feasibility of the approach and the agreement between model predictions and measurements through the above prototype experiments, we use the continuum model (and its finite element implementation) to explore the design space beyond the limitations of current fabrication constraints (Movie S4).

We start by considering a slender structure with point defects alternating on opposite surfaces (Fig. 5*A*). An impulse applied to the right end of the sample (the left end is kept fixed) excites a wave that propagates at constant speed and amplitude between defects. However, the locally circular motion around each defect collectively results in a snake-like motion of the overall structure, suggesting opportunities for utilization in soft robotic motion.

Next, to achieve functional shape morphing, we combine multiple point defects with a more complex sample shape with internal and external free boundaries. Fig. 5*B* visualizes an example whose defect and boundary arrangement leads to wave splitting and merging as well as to overall shape changes, from a sitting figure with a neutral face and hanging arms to a standing one with a smiley face and upward arms. Once the transition is initiated by an impulse at the bottom center, the front propagates vertically and splits into three waves deforming the legs and torso, then again splitting into three waves to deform the arms, and, finally, reaching and reconfiguring the head shape and facial expression (the redirection around the mouth being of similar nature as the circular motion around point defects shown previously).

Finally, we study a 3D architecture capable of supporting transition waves, created by shaping 2D multistable sheets into

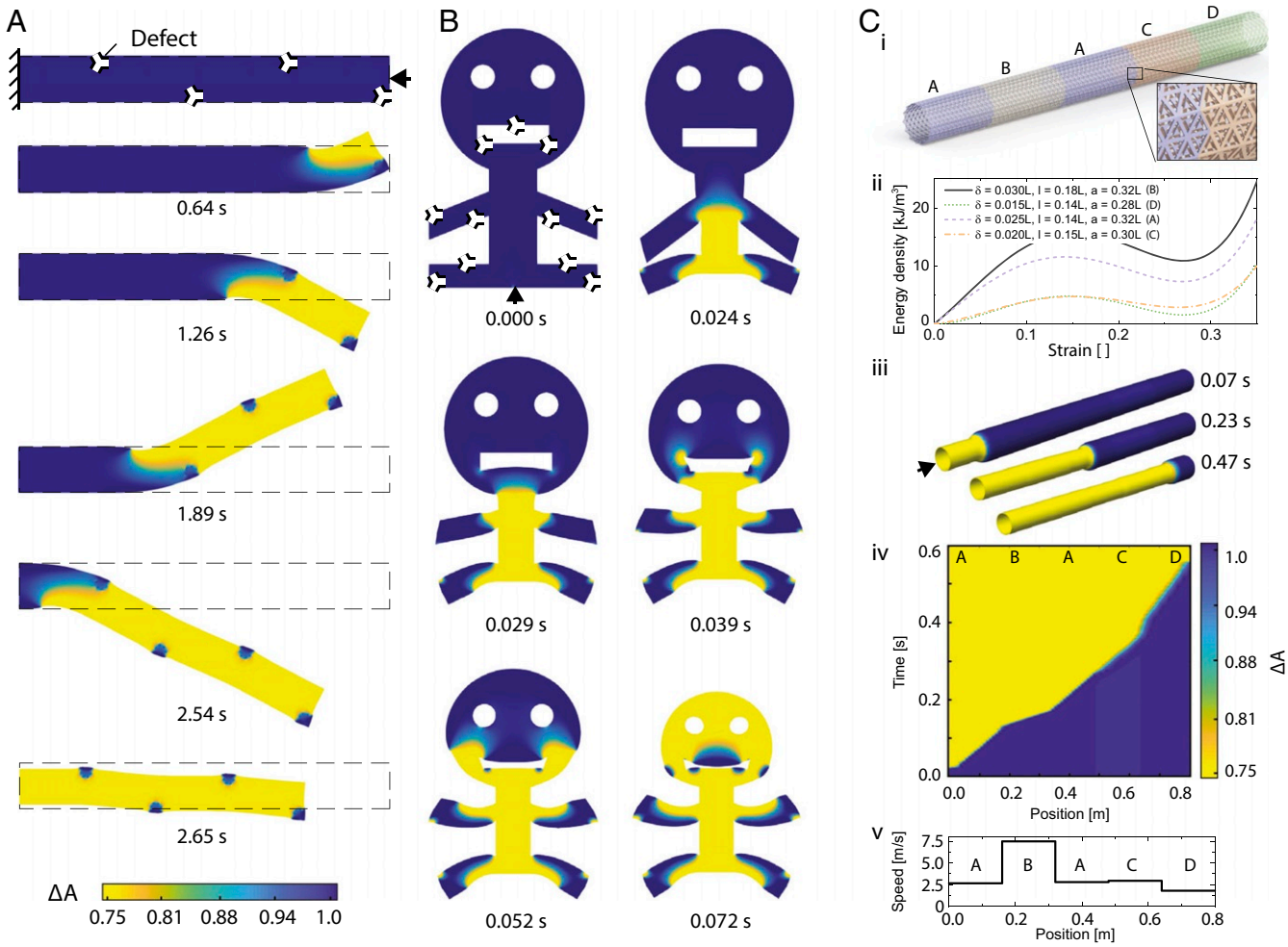

Fig. 5. The 3D waves and expansion of the design space. (*A*) By combining the effects of point defects and free surfaces, a transition fronts is designed to produce an alternating serpentine motion with potential for locomotion of soft robots. (*B*) Combining point defects with complex shapes having interior and exterior surfaces adds functionality such as splitting and merging of waves, resulting in reconfigurable devices. (*C*) Forming a 2D multistable sheet into a 3D structure: (*i*) hollow tube made of a multistable sheet; (*ii*) four different unit cell geometries produce four distinct energy landscapes, which correspond to four different wave speeds; (*iii*) simulated wave propagation at different time steps; (*iv* and *v*) quantifying the wave speed along a tube made of five sections with the above energy landscapes shows a wave that adjusts its speed in each section. The colormap shows the relative change in unit cell area; see Eq. **3**.

3D surfaces without altering the essential transition behavior or kinetics discussed in two dimensions (2D). Fig. 5*C* shows a reconfigurable circular pipe created by rolling a multistable sheet (based on the unit cell of Fig. 3) into a hollow tube. To control the wave speed along the tube, we divide it into five sections and modify the unit cell geometry in each of those. Remarkably, we find that the front seamlessly propagates from section to section, rapidly changing its speed within approximately a single unit cell when entering a new section. This is confirmed by the numerically measured speed profile (Fig. 5 *C*, *v*) with velocities ranging from 1.8 m/s to 7.45 m/s (a difference of $> 300\%$).

Summary and Conclusion

To summarize, we have demonstrated, via a combination of theory, simulations, and experiments, that periodically bistable networks show structural phase transition fronts that propagate with many of the characteristics classically known from crystalline solids, including the interaction mechanisms with lattice defects. Homogeneous networks resulted in constant-speed transition fronts (emerging from the balance between energy dissipation by damping and release of stored mechanical energy), whereas the presence of defects was shown to redirect or pin transition waves, as well as to split, delay, or merge propagating wave fronts. Unlike their crystalline counterparts, the presented structures allow for full control of the network architecture (and an efficient performance prediction through the presented continuum mechanical model), and are thus amenable to tailored wave motion and optimized reconfiguration kinetics. We further note that the behavior of the networks is robust and minimally affected by imperfections introduced during either fabrication or testing, such as broken ligaments. Like all mechanical analogs, the presented metamaterial features some but certainly not all aspects of phase transformations in solids, excluding, for example, statistical effects such as those arising from finite temperature. Admittedly, transition waves in the shown examples are one-time effects without automatic resetting; however, unlike in previous approaches (15, 18), each structural network is easily reset by applying mechanical loads to expand all unit cells—a task that can be realized, for example, using pneumatic actuators.

The multistable structures presented here serve as representative examples of the more general concept of employing structural transition fronts for guided motion and reconfiguration

in arbitrary dimensions and of arbitrary complexity. The same principles (and the same model) apply to 3D unit cells, which widens the untapped design space. Moreover, graded networks of spatially changing unit cells promise local wave speed modulation, which is of interest, for example, for mechanical logic (15, 40, 41), 4D printing (29–31), and morphing surfaces and reconfigurable devices (42–44). The simple yet powerful link between multistable energy landscape and resulting wave speed provides fruitful grounds to engage in extending concepts classically used for linear waves—such as transformation optics for wave focusing (45, 46)—to the strongly nonlinear transition front motion reported here.

Materials and Methods

Details of the materials and fabrication methods are summarized in *SI Appendix*, section 1. The experimental procedures, including the uniaxial tensile tests, microscopy, and analysis of planar waves, are described in *SI Appendix*, section 2. FEA procedures, continuum model, and numerical implementations are detailed in *SI Appendix*, section 3.

Data Availability

The data that support the findings of this study are openly available in Figshare under https://doi.org/10.6084/m9.figshare.10048724.

ACKNOWLEDGMENTS. We acknowledge support from the US Army Research Office through Award W911NF-17-1-0147. A.R. acknowledges support from Swiss National Science Foundation through Grant P3P3P2-174326. The views and conclusions contained in this document are those of the authors and should not be interpreted as representing the official policies, either expressed or implied, of the Army Research Laboratory or the US government. The US government is authorized to reproduce and distribute reprints for government purposes notwithstanding any copyright notation herein.

1. M. Kadic, T. Bückmann, R. Schittny, M. Wegener, Metamaterials beyond electromagnetism. *Rep. Prog. Phys.* **76**, 126501 (2013).
2. J. Christensen, M. Kadic, O. Kraft, M. Wegener, Vibrant times for mechanical metamaterials (book review). *MRS Commun.* **5**, 453–462 (2015).
3. K. Bertoldi, V. Vitelli, J. Christensen, M. V. Hecke, Flexible mechanical metamaterials. *Nat. Rev. Mater.* **2**, 17066 (2017).
4. M. I. Hussein, M. J. Leamy, M. Ruzzene, Dynamics of phononic materials and structures: Historical origins, recent progress, and future outlook. *Appl. Mech. Rev.* **66**, 040802 (2014).
5. S. D. Huber, Topological mechanics. *Nat. Phys.* **12**, 621–623 (2016).
6. P. Wang, L. Lu, K. Bertoldi, Topological phononic crystals with one-way elastic edge waves. *Phys. Rev. Lett.* **115**, 104302 (2015).
7. S. Zhang, C. Xia, N. Fang, Broadband acoustic cloak for ultrasound waves. *Phys. Rev. Lett.* **106**, 024301 (2011).
8. D. Elser *et al.*, Reduction of guided acoustic wave brillouin scattering in photonic crystal fibers. *Phys. Rev. Lett.* **97**, 133901 (2006).
9. T. Elnady *et al.*, Quenching of acoustic bandgaps by flow noise. *Appl. Phys. Lett.* **94**, 134104 (2009).
10. F. Casadei, L. Dozio, M. Ruzzene, K. Cunefare, Periodic shunted arrays for the control of noise radiation in an enclosure. *J. Sound Vib.* **329**, 3632–3646 (2010).
11. A. J. Zelhofer, D. M. Kochmann, On acoustic wave beaming in two-dimensional structural lattices. *Int. J. Solids Struct.* **115-116**, 248–269 (2017).
12. J. Meaud, K. Che, Tuning elastic wave propagation in multistable architected materials. *Int. J. Solids Struct.* **122**, 69–80 (2017).
13. C. Valencia, D. Restrepo, N. D. Mankame, P. D. Zavattieri, J. Gomez, Computational characterization of the wave propagation behaviour of multi-stable periodic cellular materials. *Extreme Mech. Lett.* **33**, 100565 (2019).
14. M. Schaeffer, M. Ruzzene, Wave propagation in reconfigurable magneto-elastic kagome lattice structures. *J. Appl. Phys.* **117**, 194903 (2015).
15. J. R. Raney *et al.*, Stable propagation of mechanical signals in soft media using stored elastic energy. *Proc. Natl. Acad. Sci. U.S.A.* **113**, 9722–9727 (2016).
16. R. Osama, A. F. Bilal, C. Daraio, Bistable metamaterial for switching and cascading elastic vibrations. *Proc. Natl. Acad. Sci. U.S.A.* **114**, 4603–4606 (2017).
17. B. Deng, J. Raney, V. Tournat, K. Bertoldi, Elastic vector solitons in soft architected materials. *Phys. Rev. Lett.* **118**, 204102 (2017).
18. N. Nadkarni, A. F. Arrieta, C. Chong, D. M. Kochmann, C. Daraio, Unidirectional transition waves in bistable lattices. *Phys. Rev. Lett.* **116**, 244501 (2016).
19. N. Nadkarni, C. Daraio, R. Abeyaratne, D. M. Kochmann, Universal energy transport law for dissipative and diffusive phase transitions. *Phys. Rev. B* **93**, 104109 (2016).
20. K. Bhattacharya, *Microstructure of Martensite* (Oxford University Press, Oxford, United Kingdom, 2003).
21. D. A. Porter, K. E. Easterling, M. Sherif, *Phase Transformations in Metals and Alloys* (CRC, revised reprint, 2009).
22. F. Jona, G. Shirane, *Ferroelectric Crystals, International Series of Monographs on Solid State Physics* (Pergamon, 1962).
23. F. Falk, Ginzburg-landau theory and solitary waves in shape-memory alloys. *Z. Phys. B Condens. Matter* **54**, 159–167 (1984).
24. M. Fiebig, T. Lottermoser, D. Meier, M. Trassin, The evolution of multiferroics. *Nat. Rev. Mater.* **1**, 16046 (2016).
25. J. W. Christian, S. Mahajan, Deformation twinning. *Prog. Mater. Sci.* **39**, 1–157 (1995).
26. A. Onuki, *Phase Transition Dynamics* (Cambridge University Press, 2002).
27. A. J. Bray, Theory of phase-ordering kinetics. *Adv. Phys.* **51**, 481–587 (2002).
28. M. J. Frazier, D. M. Kochmann, Atomimetic mechanical structures with nonlinear topological domain evolution kinetics. *Adv. Mater.* **29**, 1605800 (2017).
29. T. Chen, K. Shea, An autonomous programmable actuator and shape reconfigurable structures using bistability and shape memory polymers. *3D Print. Addit. Manuf.* **5**, 91–101 (2018).
30. H. Fu *et al.*, Morphable 3d mesostructures and microelectronic devices by multistable buckling mechanics. *Nat. Mater.* **17**, 268–276 (2018).
31. X. Kuang *et al.*, Advances in 4D printing: Materials and applications. *Adv. Funct. Mater.* **29**, 1805290 (2019).
32. A. Rafsanjani, D. Pasini, Bistable auxetic mechanical metamaterials inspired by ancient geometric motifs. *Extreme Mech. Lett.* **9**, 291–296 (2016).
33. X. Shang, L. Liu, A. Rafsanjani, D. Pasini, Durable bistable auxetics made of rigid solids. *J. Mater. Res.* **33**, 300–308 (2018).
34. K. Binder, Finite size effects on phase transitions. *Ferroelectrics* **73**, 43–67 (1987).
35. E. Nes, N. Ryum, O. Hunderi, On the Zener drag. *Acta Metall.* **33**, 11–22 (1985).
36. R. Abeyaratne, J. K. Knowles, Kinetic relations and the propagation of phase boundaries in solids. *Arch. Ration. Mech. Anal.* **114**, 119–154 (1991).
37. L. Truskinovsky, "Kinks versus shocks" in *Shock Induced Transitions and Phase Structures in General Media* , J. E. Dunn, R. Fosdick, M. Slemrod, Eds. (Springer, 1993), pp. 185–229.
38. J. Paulose, B. G.-g. Chen, V. Vitelli, Topological modes bound to dislocations in mechanical metamaterials. *Nat. Phys.* **11**, 153–156 (2015).
39. G. Baardink, A. Souslov, J. Paulose, V. Vitelli, Localizing softness and stress along loops in 3D topological metamaterials. *Proc. Natl. Acad. Sci. U.S.A.* **115**, 489–494 (2018).
40. Y. Jiang, L. M. Korpas, J. R. Raney, Bifurcation-based embodied logic and autonomous actuation. *Nat. Commun.* **10**, 128 (2019).
41. Y. Song *et al.*, Additively manufacturable micro-mechanical logic gates. *Nat. Commun.* **10**, 882 (2019).
42. A. Rafsanjani, Y. Zhang, B. Liu, S. M. Rubinstein, K. Bertoldi, Kirigami skins make a simple soft actuator crawl. *Sci. Rob.* **3**, eaar7555 (2018).
43. A. Rafsanjani, L. Jin, B. Deng, K. Bertoldi, Propagation of pop ups in kirigami shells. *Proc. Natl. Acad. Sci. U.S.A.* **116**, 8200–8200 (2019).
44. T. Chen, O. R. Bilal, K. Shea, C. Daraio, Harnessing bistability for directional propulsion of soft, untethered robots. *Proc. Natl. Acad. Sci. U.S.A.* **115**, 5698–5702 (2018).
45. H. Chen, C. T. Chan, P. Sheng, Transformation optics and metamaterials. *Nat. Mater.* **9**, 387–396 (2010).
46. S. R. Sklan, B. Li, A unified approach to nonlinear transformation materials. *Sci. Rep.* **8**, 4436 (2018).

PNAS
www.pnas.org

Supplementary Information for

Guided transition waves in multistable metamaterials

Lishuai Jin*, Romik Khajehtourian*, Jochen Mueller*, Ahmad Rafsanjani*, Vincent Tournat, Katia Bertoldi, Dennis M. Kochmann

Corresponding Authors: Katia Bertoldi and Dennis M. Kochmann
E-mail: bertoldi@seas.harvard.edu, dmk@ethz.ch
***L.J., R.K., J.M., and A.R. contributed equally to this work and are listed in alphabetical order.**

This PDF file includes:

Other supplementary materials for this manuscript include the following:

Supporting Information Text

1. Material and Fabrication

The material used in all structures is a thermoplastic acetal homopolymer resin (DuPont™, Midland, MI, USA) with a sheet thicknesses of $h = 1/16$ in, Young's modulus $E = 2.306\ GPa$, and Poisson's ratio ν=0.35 (Fig. S1). Structures are laser cut (Universal Laser System PLS6.150D) using the following settings: the laser power is set to maximum, the speed to 12% of the maximum, PPI to 1000, the z-movement is turned off, the laser direction set to 'both' and the flow to 'air'. As shown in Fig. S2, the laser cutting process results in cuts with widths varying from approximately $w_b = 100\ \mu$m on the bottom face to $w_t = 600\ \mu$m on the top face. Point defects are introduced into the structure by inserting the negative of an open unit cell, i.e. filling the gaps of the open unit cell with a structure fabricated from transparent, acrylic sheets of $h = 1/8$ in (McMaster-Carr, Elmhurst, IL, USA) to prevent the unit cell from collapsing into its low-energy equilibrium state.

2. Experiments

A. Uniaxial Tension Tests. Uniaxial tensile and compression tests (Figs. S4-S8) are performed on a universal testing machine (Universal Testing Machine 5969, Instron, Norwood, MA, USA) according to ASTM D638-10. We first test the mechanical properties of the material using dogbone specimens with a test speed of 10 mm/min (specimen type IV; see Fig. S1). The results of these tests are used as an input to calibrate both the finite element (FE) and continuum models. Tensile/compression tests of the different multistable structures are performed at the same speed. To allow for transverse movement, required when testing structures with two or more columns under uniaxial tension, the samples were mounted in a test rig containing horizontal slots and two roller bearings for each joint (Fig. 1).

B. Microscopy. The unit cell geometry and laser cutting quality shown in Fig. S2 is analyzed via light microscopy (Keyence VHX 6000, Osaka, Osaka Prefecture, Japan) using a VH-Z20R ultra-small, high-performance zoom lens with a zoom range of 20× to 200×. Vertical images are stacked and processed by the software to create a 3D profile of the hinges and cuts.

C. Analysis of Planar Waves. Planar wave experiments are conducted on a flat acrylic plate with a second transparent acrylic plate placed above the samples to avoid any out-of-plane motion during the tests. During these tests we record the motion of the structures using a high-speed camera (SONY RX100V) at a frame rate of 480 fps and extract their local deformation using an open-source digital image correlation (DIC) and tracking package (1). We place a black circular marker at the center of each unit cell to track their positions and use that data to quantify the deformation through the relative change in area (see Eq. (1) in the manuscript).

3. Modeling

The modeling consists of two parts. FEA are used to simulate individual unit cells and small tessellations thereof (to complement the above experiments) with the objective of extracting the effective stress-strain curve and the stored energy density ψ as a function of deformation under periodic boundary conditions. Results of the FE models (i.e., the energy density ψ for a specific unit cell design) are fed into a continuum model, which has been developed for the efficient description of the time-dependent behavior of multistable structures and to explore the design space. Both models are described in the following.

A. Finite Element Simulations. To extract the effective mechanical response of a single unit cell, FEA are conducted using the commercial software package ABAQUS 6.14/Standard (Dassault Systèmes, Vélizy-Villacoublay, France). The Delrin base material of all structures is described by an elastic-plastic constitutive model, whose parameters are calibrated by comparison to the uniaxial tensile test data (Fig. S1). Each structure is discretized using finite-strain quadratic plane-stress elements (CPS8R and CPS6) and loaded by strain-driven periodic boundary conditions for the extraction of the homogenized stress-strain response. Localized penetration of structural features is avoided by modeling frictionless contact through a penalty constraint enforcement method with nonlinear stiffness in the normal contact direction. To promote convergence when contact is present, a dynamic implicit solver is used with moderate dissipation to determine the quasistatic response. The effect of unit cell geometry on its mechanical response is assessed through parameter studies using the Python scripting interface of ABAQUS. A laser beam thickness of 0.2 mm, which affects the fabricated geometries, is accounted for in the simulations (Fig. S2).

B. Continuum model. Inspired by constitutive models for phase transformations in solids, we propose a continuum model to describe the effective mechanical behavior behind the transition waves in multistable networks, which operates efficiently at the continuum level (hence being applicable to large structures) while taking into account information about the structural architecture in a homogenized fashion.

Supported by experiments, we neglect the effects of friction (the ground is smooth and the structure is assumed to slide freely), and we assume that inertial effects are negligible compared to the dissipation in the system. The latter stems from the viscoelastic response of the base material and is indeed required to produce constant-speed transition waves (2) (in a nutshell, the energy release from the bistable potential upon each snapping event is consumed by the viscous dissipation associated with the base material's deformation in response to the snapping event).

To describe the mechanical response of a sample made of the multistable structural architecture, we take a variational approach and define a strain energy density W which characterizes the effective constitutive behavior. For convenience, we adhere to linearized kinematics to describe the deformation by the symmetric infinitesimal strain tensor $\boldsymbol{\varepsilon}$, which can be decomposed into a purely volumetric contribution, $\theta = \mathrm{tr}(\boldsymbol{\epsilon})/d$, and a deviatoric (i.e., volume-preserving) contribution, $\boldsymbol{e} = \boldsymbol{\varepsilon} - \theta \boldsymbol{I}$. (The extension to finite strains is technically straight-forward, yet we expect no new physics so the linearized description is chosen here for illustrative simplicity.) Observing that the bistability of a unit cell is of volumetric nature (the two equilibrium states are characterized by the open and closed configurations, distinguished by a volumetric strain), we assume that the strain energy density is of the additive form

$$W(\boldsymbol{\varepsilon}) = \psi(\theta) + W_{\mathrm{dev}}(\boldsymbol{e}) = \psi(\theta) + \frac{\mu}{2} \|\boldsymbol{e}\|^2 , \qquad [1]$$

where

$$\psi(\theta) = c_0 + c_1\theta + c_2\theta^2 + c_3\theta^3 + c_4\theta^4 \qquad [2]$$

is an equation of state which is here linked to the non-convex potential energy density of a unit cell (calculated by FEA, see above, and fitted to a quartic polynomial for ease of analytical differentiation). $W_{\mathrm{dev}}(\boldsymbol{e}) = \frac{\mu}{2} \|\boldsymbol{e}\|^2$ represents an effective energy density penalizing changes in deformation between neighboring unit cells. This latter energy contribution vanishes within homogeneous domains (where all unit cells deform in the same volumetric fashion), so it only arises in and close to domain boundaries and hence stands for an effective interface energy density with a phenomenological

modulus $\mu > 0$. We acknowledge that the above energy density is, of course, not the only possible form to describe the transition front behavior. However, it accurately and efficiently captures the salient features observed in experiments and is therefore used here.

By following classical Coleman-Noll theory, the associated infinitesimal stress tensor, describing the bistable elastic response, follows as

$$\boldsymbol{\sigma}_{\mathrm{e}} = \frac{\partial W}{\partial \boldsymbol{\varepsilon}} = \frac{\psi'(\theta)}{d}\boldsymbol{I} + \mu \boldsymbol{e}. \qquad [3]$$

In addition to the above elastic contribution to the stress tensor, the viscoelastic nature of the base material causes viscous stresses that counter deformation in a time-dependent fashion. As a leading-order approximation, we here assume linear viscosity and introduce a viscous stresses tensor contribution $\boldsymbol{\sigma}_{\mathrm{v}} = \eta \dot{\boldsymbol{\varepsilon}}$ with a Newtonian viscosity parameter $\eta \geq 0$ (non-negative by the second law of thermodynamics), and dots denoting time derivatives. Overall, the stress tensor thus becomes

$$\boldsymbol{\sigma} = \boldsymbol{\sigma}_{\mathrm{e}} + \boldsymbol{\sigma}_{\mathrm{v}} = \frac{\psi'(\theta)}{d}\boldsymbol{I} + \mu \boldsymbol{e} + \eta \dot{\boldsymbol{\varepsilon}}. \qquad [4]$$

The time-dependent deformation of the body on the macroscale is governed by the conservation of linear momentum (in the absence of body forces and with negligible inertia), which requires

$$\operatorname{div} \boldsymbol{\sigma} = \boldsymbol{0} \qquad \Leftrightarrow \qquad \operatorname{div}\left(\frac{\psi'(\theta)}{d}\boldsymbol{I} + \mu \boldsymbol{e} + \eta \dot{\boldsymbol{\varepsilon}}\right) = \boldsymbol{0}. \qquad [5]$$

By assuming that μ and η are constant material parameters, the above is equivalent to

$$\frac{1}{d}\left(\frac{\psi''(\theta)}{d} - \mu\right) \operatorname{grad}(\operatorname{tr} \boldsymbol{\varepsilon}) + \mu \operatorname{div} \boldsymbol{\varepsilon} + \eta \operatorname{div} \dot{\boldsymbol{\varepsilon}} = \boldsymbol{0}. \qquad [6]$$

Invoking the strain–displacement relation $\boldsymbol{\varepsilon} = \operatorname{sym}(\nabla \boldsymbol{u})$ with the displacement field $\boldsymbol{u} : \Omega \to \mathbb{R}^d$ defined across a macroscopic body Ω, we transform Eq. (6) into

$$\frac{\eta}{2}(\dot{u}_{i,kk} + \dot{u}_{k,ki}) + \left(\frac{\psi''(u_{k,k}/d)}{d^2} - \frac{\mu}{d}\right) u_{k,ki} + \frac{\mu}{2}(u_{i,kk} + u_{k,ki}) = 0, \qquad [7]$$

where we used index notation with Einstein's summation convention and subscripts following a comma denoting partial derivatives with respect to spatial coordinates.

The system of partial differential equations Eq. (7) is solved with given boundary conditions, using an in-house finite element code which discretizes the 2D bodies of interest by a regular mesh of linear triangular (CST) elements and uses a backward-Euler scheme for implicit time integration with a time step size Δt (using a Newton-Raphson iterative solver).

The link between this continuum description of a sample and the characteristics of the underlying unit cell is established explicitly through the interaction potential ψ (defining the interaction energy in any link between unit cells) and implicitly through modulus μ and viscosity η. The latter two parameters are introduced as an efficient means to capture the large-scale behavior. We turn to homogenization theory to link those model parameters to the unit cell specifics (the procedure can generally be applied to other unit cells and is not limited to the specific design employed here). Following first-order homogenization, we assume that any macroscale deformation state, characterized by a strain tensor $\boldsymbol{\varepsilon}$, results in an affine deformation of the microscale unit cell deforming by the same homogeneous strains $\boldsymbol{\varepsilon}$ (rigid-body motion being irrelevant here due to negligible inertia). Since

unit cells are arranged in a triangular lattice, which is generally characterized by stiff, stretching-dominated behavior, the affine deformation assumption – though generally providing only an upper bound – is a realistic leading-order approximation.

We consider a unit cell Ω with volume V, which is connected to its six neighboring unit cells. Without loss of generality, we choose the center of the unit cell at $\boldsymbol{x}_0 = \boldsymbol{0}$ to be the origin of the local coordinate frame, so that the affine deformation of the unit cell (characterized by a volumetric expansion with volumetric strain θ and superimposed strains $\boldsymbol{\epsilon}$) imposes displacements $\boldsymbol{u}(\boldsymbol{x}) = (\theta\boldsymbol{I} + \boldsymbol{\epsilon})\boldsymbol{x} = \boldsymbol{\varepsilon}\boldsymbol{x}$. Consequently, the displacement of the center of the α-th neighboring unit cell ($\alpha = 1, \dots, 6$), originally located at $\boldsymbol{x}_\alpha$, is $\boldsymbol{u}_\alpha = (\theta\boldsymbol{I} + \boldsymbol{\epsilon})\boldsymbol{x}_\alpha$. We further note that the undeformed distance vector from the origin to each neighboring unit cell center is $\boldsymbol{x}_\alpha - \boldsymbol{x}_0 = \boldsymbol{x}_\alpha$, while the corresponding deformed distance vector is given by

$$\boldsymbol{r}_\alpha = \boldsymbol{u}_\alpha + \boldsymbol{x}_\alpha - (\boldsymbol{x}_0 + \boldsymbol{u}_0) = \boldsymbol{u}_\alpha + \boldsymbol{x}_\alpha = [(\theta + 1)\boldsymbol{I} + \boldsymbol{\epsilon}]\boldsymbol{x}_\alpha = (\boldsymbol{\varepsilon} + \boldsymbol{I})\boldsymbol{x}_\alpha. \tag{8}$$

We define the effective energy density of a unit cell Ω undergoing strains $\boldsymbol{\varepsilon}$ as the average energy density

$$W_\Omega(\boldsymbol{\varepsilon}) = \frac{1}{2}\sum_{\alpha=1}^{6} \psi(\varepsilon_\alpha), \tag{9}$$

where ψ represents the elastic interaction energy dependent on the 1D strains $\varepsilon_\alpha = (\|\boldsymbol{r}_\alpha\| - \|\boldsymbol{x}_\alpha\|)/\|\boldsymbol{x}_\alpha\|$ in each link between unit cell Ω and its six neighboring unit cells. Inserting the above macro-to-micro transition relations hence yields

$$\varepsilon_\alpha = \frac{\|\boldsymbol{r}_\alpha\| - \|\boldsymbol{x}_\alpha\|}{\|\boldsymbol{x}_\alpha\|} = \frac{\|\boldsymbol{r}_\alpha\|}{\|\boldsymbol{x}_\alpha\|} - 1 = \|(\boldsymbol{\varepsilon} + \boldsymbol{I})\hat{\boldsymbol{x}}_\alpha\| - 1 \tag{10}$$

where $\hat{\cdot} = (\cdot)/\|\cdot\|$ denotes a unit vector. We note that the factor $1/2$ in Eq. (9) corrects for double-counting of each interaction link when composing the total energy of the network.

Differentiating the effective energy density yields the effective elastic stress tensor and its components:

$$\boldsymbol{\sigma}_\mathrm{e} = \frac{\partial W_\Omega}{\partial \boldsymbol{\varepsilon}} \qquad \Rightarrow \qquad \sigma_{ij} = \frac{1}{2}\sum_{\alpha=1}^{6} \frac{\partial \psi}{\partial \varepsilon}(\varepsilon_\alpha)\frac{\partial \varepsilon_\alpha}{\partial \varepsilon_{ij}}, \tag{11}$$

and the incremental stiffness tensor of fourth order is derived analogously, having components

$$\mathbb{C} = \frac{\partial \boldsymbol{\sigma}_\mathrm{e}}{\partial \boldsymbol{\varepsilon}} \qquad \Rightarrow \qquad \mathbb{C}_{ijkl} = \frac{1}{2}\sum_{\alpha=1}^{6}\left[\psi''(\varepsilon_\alpha)\frac{\partial \varepsilon_\alpha}{\partial \varepsilon_{ij}}\frac{\partial \varepsilon_\alpha}{\partial \varepsilon_{kl}} + \psi'(\varepsilon_\alpha)\frac{\partial^2 \varepsilon_\alpha}{\partial \varepsilon_{ij}\,\partial \varepsilon_{kl}}\right]. \tag{12}$$

The derivatives in Eq. (11) and Eq. (12) can be expressed, using Eq. (10) and exploiting the symmetry of the strain tensor, as

$$\frac{\partial \varepsilon_\alpha}{\partial \varepsilon_{ij}} = \frac{1}{2}\left[(\hat{\boldsymbol{r}}_\alpha)_i(\hat{\boldsymbol{x}}_\alpha)_j + (\hat{\boldsymbol{x}}_\alpha)_i(\hat{\boldsymbol{r}}_\alpha)_j\right], \tag{13}$$

writing $(\boldsymbol{x})_i$ for the i-th component of vector $\boldsymbol{x}$. Analogously, we arrive at

$$\begin{aligned}\frac{\partial^2 \varepsilon_\alpha}{\partial \varepsilon_{ij}\,\partial \varepsilon_{kl}} = \frac{1}{2}\Big[&(\delta_{ik}(\hat{\boldsymbol{r}}_\alpha)_l(\hat{\boldsymbol{x}}_\alpha)_j + \delta_{jk}(\hat{\boldsymbol{x}}_\alpha)_i(\hat{\boldsymbol{r}}_\alpha)_l) \\ &- \frac{1}{2}\left((\hat{\boldsymbol{r}}_\alpha)_i(\hat{\boldsymbol{x}}_\alpha)_j + (\hat{\boldsymbol{x}}_\alpha)_i(\hat{\boldsymbol{r}}_\alpha)_j\right)\Big((\hat{\boldsymbol{r}}_\alpha)_k(\hat{\boldsymbol{r}}_\alpha)_l + (\hat{\boldsymbol{r}}_\alpha)_k(\hat{\boldsymbol{r}}_\alpha)_l\Big)\Big].\end{aligned} \tag{14}$$

In order to reconcile the empirical energy density formulated in Eq. (1) with the homogenized energy density Eq. (9) (and to reduce Eq. (9) to a simple analytical expression), we exploit that the volumetric deformation is essential in capturing the bistability, while deviatoric effects primarily affect domain boundary regions. To this end, we use the decomposition

$$\boldsymbol{\varepsilon} = \theta \boldsymbol{I} + \boldsymbol{\epsilon} \tag{15}$$

and expand the homogenized energy density $W_\Omega(\boldsymbol{\varepsilon}) \equiv W_\Omega(\theta, \boldsymbol{\epsilon})$ from Eq. (9) about $\boldsymbol{\varepsilon} = \theta \boldsymbol{I}$ up to quadratic order in $\boldsymbol{\epsilon}$:

$$\begin{aligned} W_\Omega &= W_\Omega(\theta, \mathbf{0}) + \frac{\partial W_\Omega}{\partial \varepsilon_{ij}}(\theta, \mathbf{0})\, \epsilon_{ij} + \frac{1}{2} \frac{\partial^2 W_\Omega}{\partial \varepsilon_{ij}\, \partial \varepsilon_{kl}}(\theta, \mathbf{0})\, \epsilon_{ij} \epsilon_{kl} + \text{h.o.t.} \\ &= W_\Omega(\theta, \mathbf{0}) + \sigma_{ij}(\theta, \mathbf{0}) \epsilon_{ij} + \frac{1}{2} \mathbb{C}_{ijkl}(\theta, \mathbf{0}) \epsilon_{ij} \epsilon_{kl} + \text{h.o.t.} \end{aligned} \tag{16}$$

Towards a numerically convenient simplification (which also admits a cleaner interpretation), we choose $\theta = \theta_0 = \text{const.}$ and hence evaluate the above expansion about the undeformed ground state. This leads to $\psi'(\theta_0) = 0$ and $\boldsymbol{x}_\alpha = \boldsymbol{r}_\alpha$, and hence

$$W_\Omega \approx W_\Omega(\theta_0, \mathbf{0}) + \frac{1}{4} \psi''(\theta_0) \sum_{\alpha=1}^{n} (\hat{\boldsymbol{x}}_\alpha)_i (\hat{\boldsymbol{x}}_\alpha)_j (\hat{\boldsymbol{x}}_\alpha)_k (\hat{\boldsymbol{x}}_\alpha)_l\, \epsilon_{ij} \epsilon_{kl} = \psi(\theta) + \frac{1}{2} \epsilon_{ij} \mathbb{C}^{\text{approx.}}_{ijkl} \epsilon_{kl} \tag{17}$$

with the approximated stiffness tensor

$$\mathbb{C}^{\text{approx.}}_{ijkl} = \frac{1}{2} \psi''(\theta_0) \sum_{\alpha=1}^{6} (\hat{\boldsymbol{x}}_\alpha)_i (\hat{\boldsymbol{x}}_\alpha)_j (\hat{\boldsymbol{x}}_\alpha)_k (\hat{\boldsymbol{x}}_\alpha)_l. \tag{18}$$

The obtained homogenized energy density Eq. (17) is analogous to the empirical energy density Eq. (1). (Of course, the resulting model will depend on the choice of θ_0 in the above expansion; results show convincing agreement between experimental data and numerical predictions for this particular choice made here.)

For the 2D triangular lattice configuration chosen here, the components of the above contribution to the stiffness tensor evaluate to

$$\mathbb{C}^{\text{approx.}}_{ijkl} = \tilde{\lambda} \delta_{ij} \delta_{kl} + \tilde{\mu} (\delta_{ik} \delta_{jl} + \delta_{il} \delta_{jk}) \qquad \text{with} \qquad \tilde{\lambda} = \tilde{\mu} = \frac{3}{8} \psi''(\theta_0)\,. \tag{19}$$

This is the classical form of isotropic linear elasticity. The empirical continuum model introduced in Eq. (1) replaces $\tilde{\lambda}$ by the bistable equation of state for the volumetric contribution. The above shows that a reasonable choice for the empirical modulus μ introduced in Eq. (1) is given by $\mu = \frac{3}{8} \psi''(\theta_0)$.

Finally, the second model parameter, the viscosity η, depends on the properties of the polymeric base material and is harder to quantify. However, it directly governs the speed and kinetics of the domain evolution process, so that η can be quantified by fitting to experimental data – which is the approach that was chosen for all simulations here. All model parameters used for simulations are summarized in Table S1.

Simulations using the continuum model were conducted using an in-house FE code; initial boundary value problems were solved by a Newton-Raphson solver. We used triangular (CST) elements for all 2D simulations and confirmed mesh convergence through h-refinement. Point defects were implemented through stiff bar elements (approximating rigid links). The tube simulation in Fig. 5c was performed by meshing a thin-walled hollow tube with tetrahedral (CST) solid elements in 3D and using the above empirical material model with $d = 3$.

Figure number	constants of Eq. (2), i.e., $\{c_0, c_1, c_2, c_3, c_4\}$	viscosity per time step, $\eta/\Delta t$	empirical shear modulus μ
Figure 3	$\{0, 0.0085, 0.641, -4.1456, 6.8689\} \times 10^6$	0.673×10^6	1.923×10^6
Figure 4	$\{0, 0.010, 0.705, -4.70, 7.89\} \times 10^6$	0.673×10^6	2.115×10^6
Figure 5a	$\{0, 0.016, 0.6058, -4.6426, 8.6121\} \times 10^6$	1.810×10^5	1.210×10^6
Figure 5b	$\{0, 0.127, 0.7556, -8.6, 17.082\} \times 10^6$	1.210×10^6	1.511×10^6
Figure 5c (A)	$\{0, 0.124, 0.2054, -5.18, 11.443\} \times 10^6$	0.724×10^6	0.411×10^6
Figure 5c (B)	$\{0, 0.127, 0.7556, -8.6, 17.082\} \times 10^6$	0.724×10^6	1.511×10^6
Figure 5c (C)	$\{0, 0.016, 0.6058, -4.6426, 8.6121\} \times 10^6$	0.724×10^6	1.212×10^6
Figure 5c (D)	$\{0, 0.0045, 1.0, -6.9, 12.36\} \times 10^6$	0.724×10^6	2.000×10^6

Table S1. Values of all parameters used by the continuum model. We point out that, while Fig. 4 was generated using a constant set of parameters, results in Fig. 3 used a slightly modified parameter set, as indicated above, to account for the free-surface effects in the finite structure used in experiments. Parameters for Fig. 5c have been chosen, as shown above, to produce the reported variations in transition front speed.

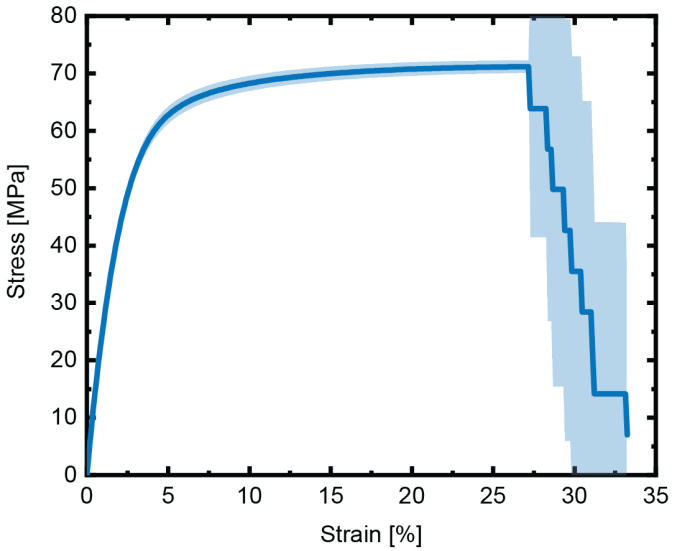

Fig. S1. Tensile test results from dogbone specimens (ASTM D638, type IV) tested on a universal testing machine. The curve shows the mean of the n=10 samples (solid line) and their standard deviation (shaded area). Note that all samples failed catastrophically; the stepwise failure of the mean curve is due to averaging over all samples.

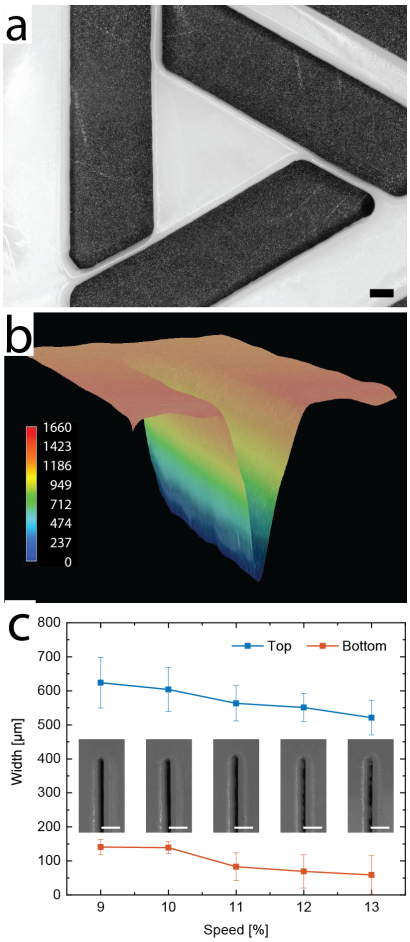

Fig. S2. Analysis of the cut geometry as fabricated by a laser cutter: (a) top view showing a unit cell's features, using a light microscope. (b) A 3D depth scan of the cut gap shows an increasing width from the bottom to the top. Note that the bottom of the gap starts at around 400 μ m. (c) Quantitative analysis of the 3D depth profiles from microscopy. Statistically averaged over five tested samples.

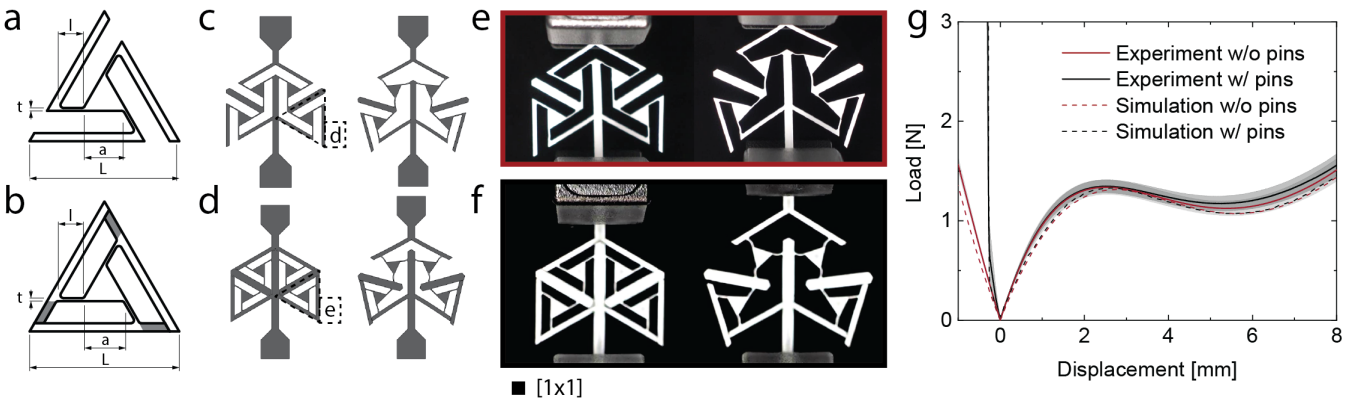

Fig. S3. Effect of pins on the mechanical properties of the unit cells: (a,b) unit cell features with and without pins; (c,d) both geometries are embedded in a dogbone specimen geometry and tested numerically in compression and tension; (e,f) experimental uniaxial tensile tests of the two specimen types show a qualitatively similar deformation behavior; (g) quantitative analysis shows a similar behavior in the tensile regime (positive displacement), but a noticeable difference in the compression regime (negative displacement), where the unit cell with pins is considerably stiffer. The shading illustrates the standard deviation calculated from 5 samples.

Fig. S4. Different unit cell tessellations tested in uniaxial tension. The combinations range from one row to three rows and from one column to three columns, covering the monostable and multistable regions as well as the transition region, shown in the phase map in Fig. S8.

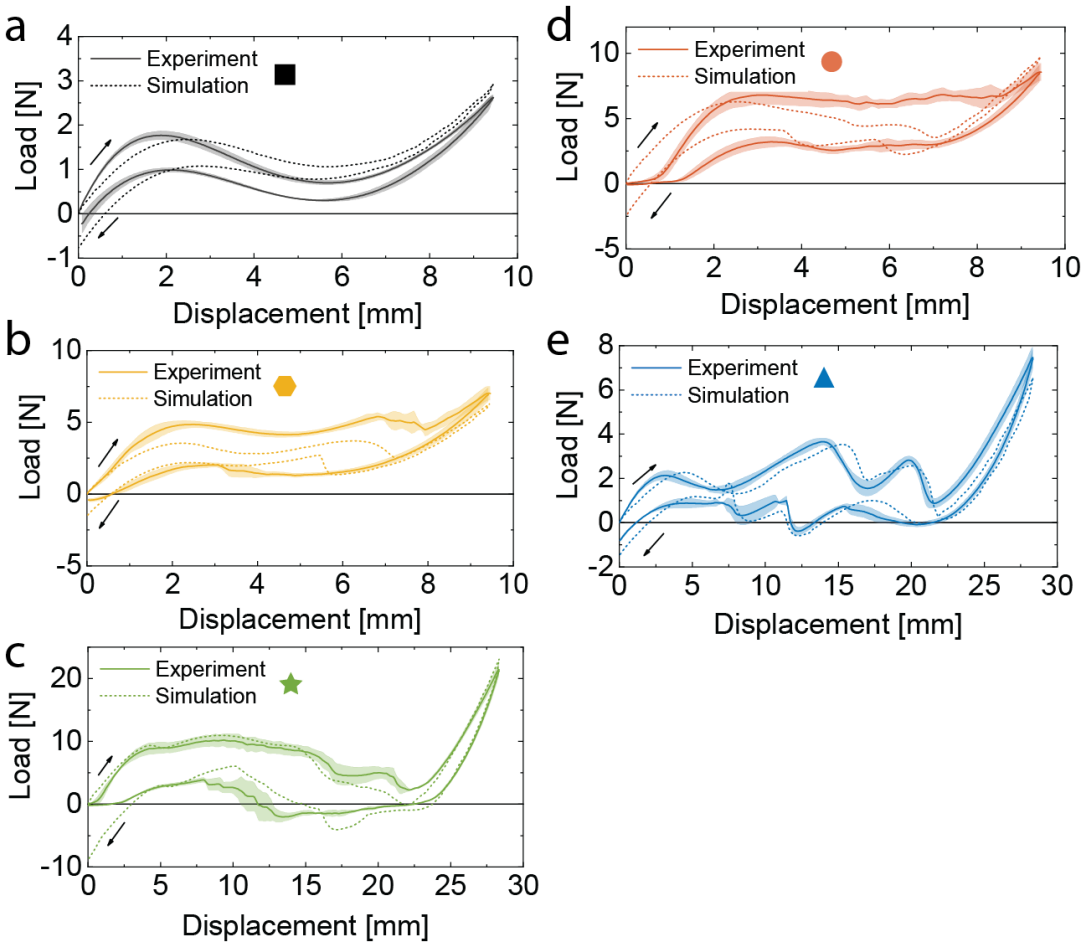

Fig. S5. Quantitative analysis of the uniaxial tensile tests shown in Fig. S4. The five cases refer to the tessellations in Fig. S4 (indicated by the symbols): (a) 1×1 unit cell, (b) 2×1 unit cell, (c) 3×3 unit cell, (d) 3×1 unit cell, and (e) 1×3 unit cell, where the first number refers to the number of (vertical) columns and the second number to the number of (horizontal) rows.

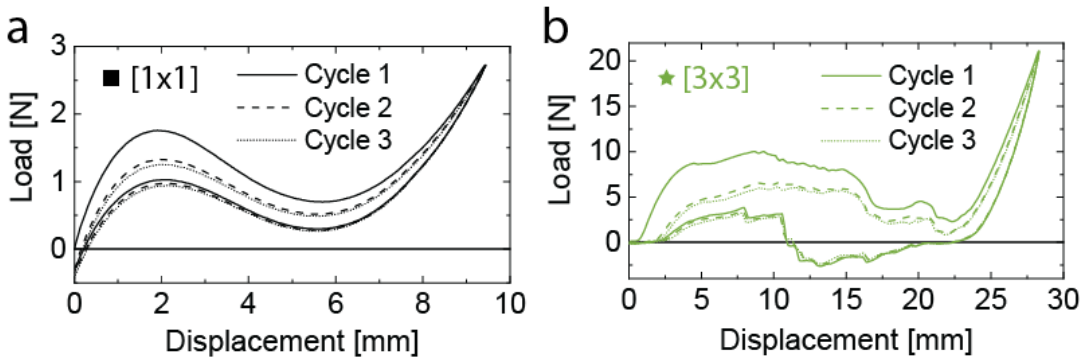

Fig. S6. Representative curves of three consecutive cycles from the experimental uniaxial tensile tests shown in Fig. S4. (a) 1×1 unit cell, (b) 3×3 unit cell. Some level of plastic deformation (localized near the hinges) is inevitable during the initial cycles, but the cyclic response stabilizes soon after the first cycle, as shown.

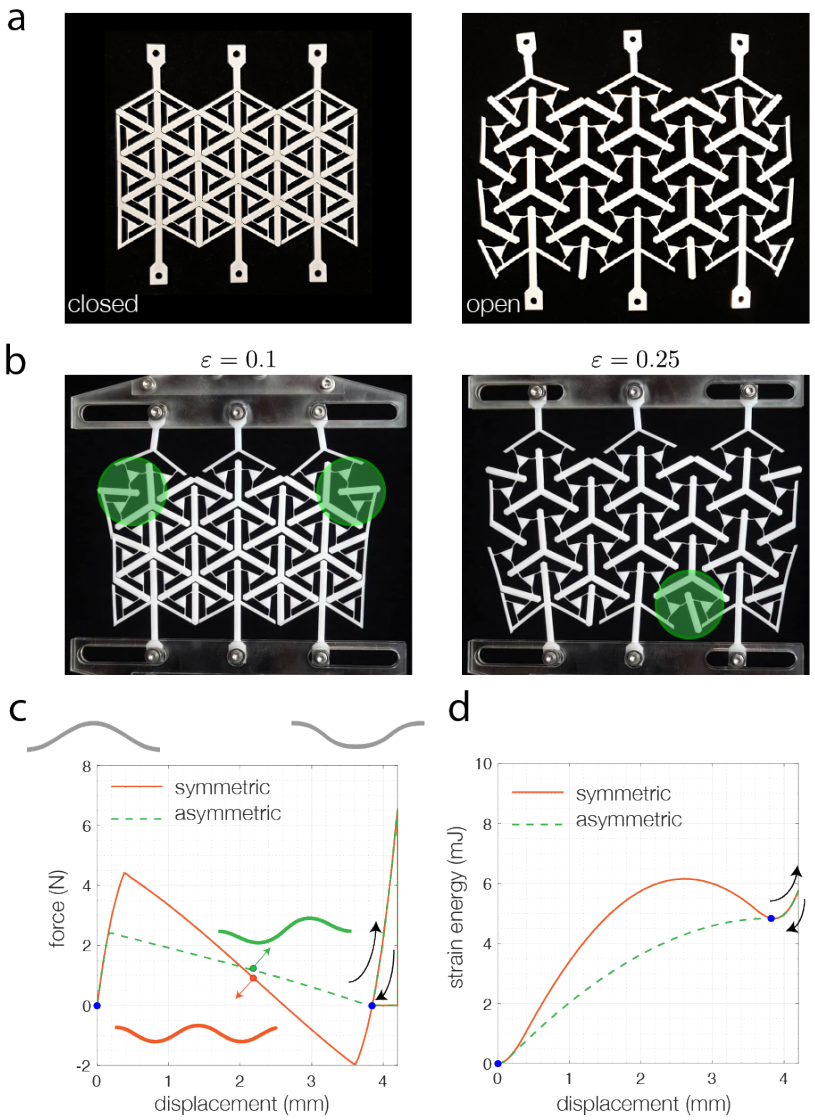

Fig. S7. (a) closed and open states of the 3×3 structure, both of which are stable (despite the load-displacement curve remaining above zero in our experiments - see Fig. S5-c). (b) This behavior can be attributed to asymmetric deformation modes triggered during loading. (c)-(d) To demonstrate this point, we focus on a simple elastic curved beam with profile described by $y = A/2[1 - \cos(2\pi x/L)]$ ($x \in [0,\ L]$) and square cross-section of edge h. Such a beam is known to be bistable when it is subjected to a mid-point displacement if $A/h > 2.31$ (3). We choose $L = 10$ mm, $A = 2$ mm and $h = 0.67$ mm (so that $A/h = 3 > 2.31$) and conduct finite elements with ABAQUS to capture its response. Specifically, we mesh the beam using 2D Timoshenko beam elements and use an isotropic linear elastic constitutive model to capture the response of the material (with Young's modulus $E = 3.85$ GPa and Poisson's ratio $\nu = 0.4$). We impose a vertical displacement, $u_z = 4.2$ mm, to its middle point and use an implicit dynamics solver to follow its deformation. Finally, we deactivate the imposed displacement and verify that the deformed configuration is stable by examining if the structure maintains its deformed shape. In our first simulation we constrain the horizontal displacement of the central point as we apply u_z. In this case the beam follows a symmetric deformation path and, as expected, the measured force is characterized by a negative region (see red line in (c)) and the strain energy shows two clear local minima (see red line in (d)). By contrast, when we remove the horizontal constraint at the central point, the beam follows an asymmetric deformation path to reach the final configuration (see green insert in (c)). In this case the measured force is always positive (see the green line in (c)) and approaches zero only at a specific point. Moroever, the strain energy at that point shows an extremum without a distinct energy barrier (see green line in (d)). However, the beam remains in the deformed configuration when the force is removed – a clear indication of bistability. As such, this simple example demonstrates that an asymmetric deformation mode can bring a structure to another stable configuration without reversing the sign of the force.

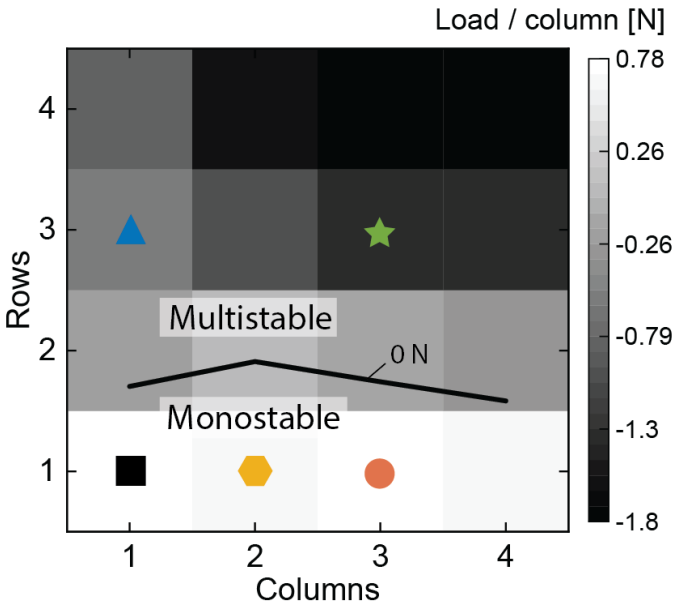

Fig. S8. Phase diagram extracted from uniaxial tensile tests (including the ones shown in Figs. S4 and S5). The diagram shows a distinct monostable region for structures with one row and a distinct multistable behavior for structures with three or more rows. It is further seen that an increasing number of columns is beneficial for multistability, as measured by the relative load (per column) of the lowest valley value (bi-/multistable if negative).

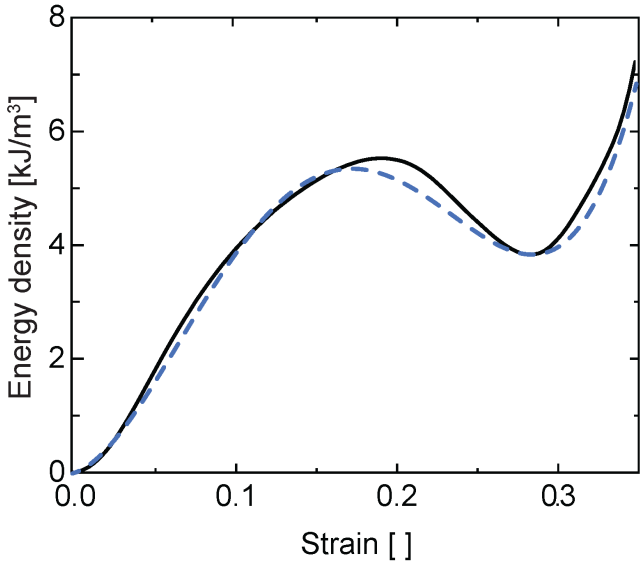

Fig. S9. Strain energy density ψ vs. volumetric expansion strain, as extracted from FEA (solid line) and as used in the continuum model (dashed line). The latter is a best-fit quartic polynomial of the former. This potential is used for simulations in Fig. 3. The other potentials used in Figs. 4 and 5 are analogous (see the polynomial coefficients in Table 1).

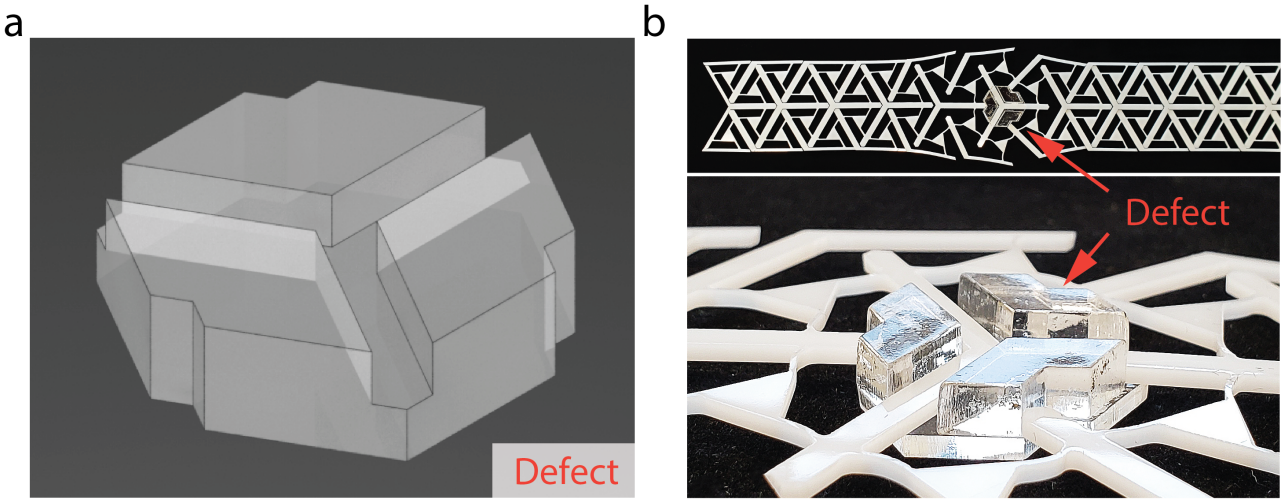

Fig. S10. Zoom-in of the defect that prevents unit cells from collapsing. a) cartoon rendering. b) photograph showing the transparent defect with the area around the defect being expanded.

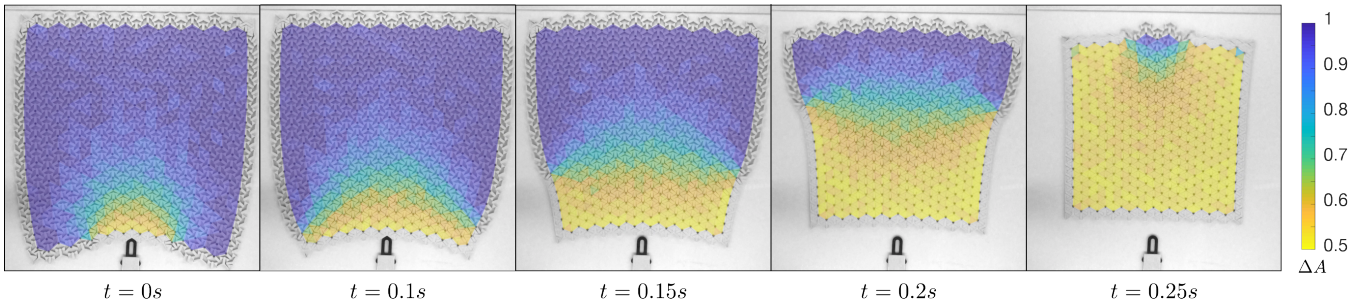

Fig. S11. Snapshots of propagation of transition wave in a larger 2D sample showing a curved front (see Movie S5).

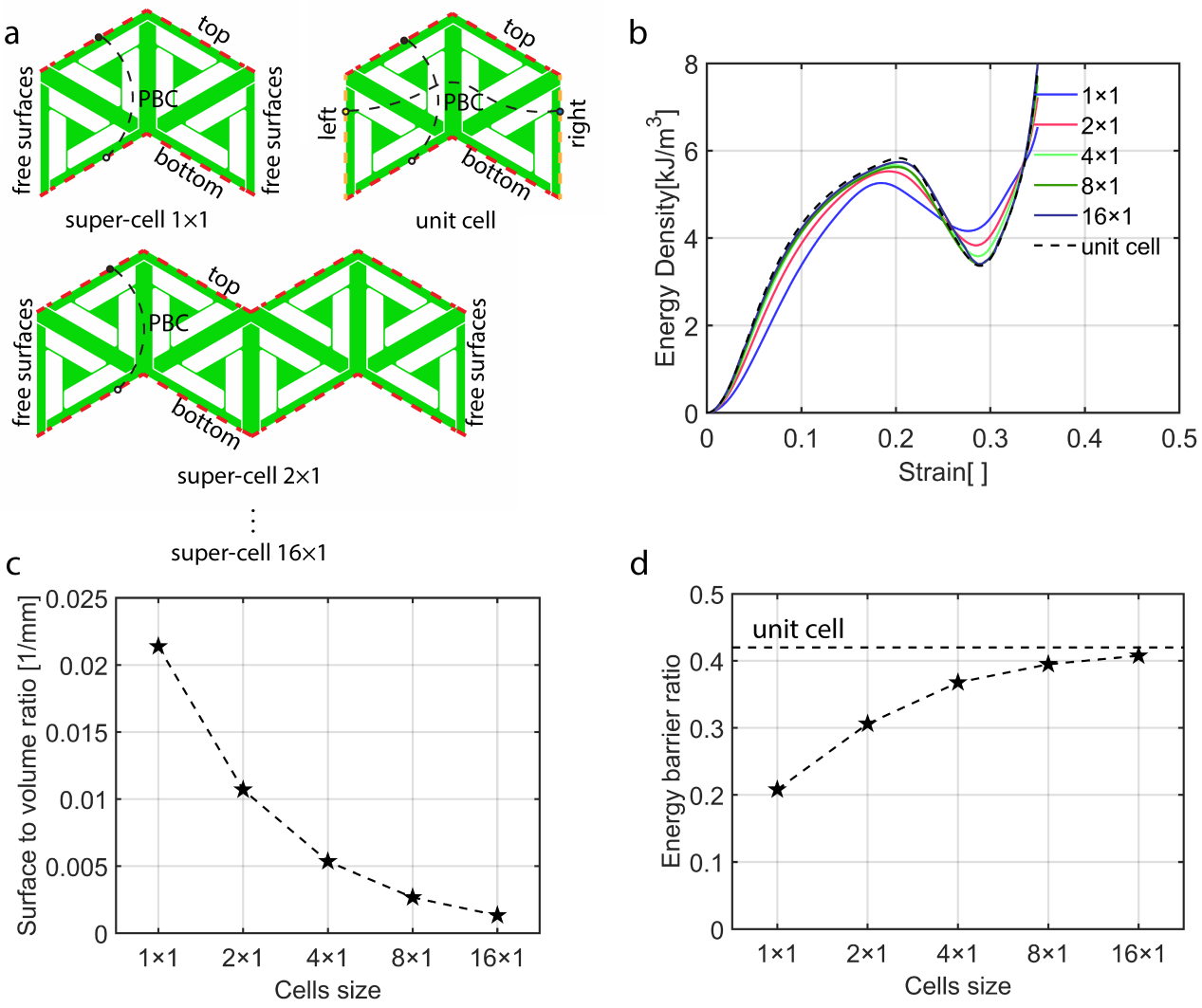

Fig. S12. Illustration of free surface effects. (a) To better illustrate the effect of free surfaces, we simulated the response of a 1×1 unit cell with periodic boundary conditions (PBCs) applied on all edges and super-cells comprising 1×1, 4×1, 8×1 and 16×1 units with PBCs applied only at their bottom and top edges. For such super-cells the vertical edges are free, so that these results allow us to investigate the surface effects. (b) Evolution of the strain energy density as a function of strain for all considered cells. (c) Surface-to-volume ratio for all considered cells. (d) Ratio of well energy to energy barrier for all considered cells. We find that, if the super-cell is sufficiently small (i.e., if the ratio of surface to volume is sufficiently large), the free surfaces affect the strain energy as well as the energy barrier ratio. Conversely, the effect of free surfaces loses importance as the number of units in the super-cell increases, and for sufficiently large super-cells the strain energy converges to that of the periodic unit cell. These results demonstrate that for structures of limited size the strain energy density function used in the continuum model is to be adjusted to account for the effect of free surfaces (as opposed to modeling the bulk response). For structures with rectangular geometry we can directly use these results to identify the strain energy to be used in the continuum model (while for more complex shapes with free surfaces further calibration of the parameters may be required).

Movie S1. Guiding transition front

Experimental demonstration of guided transition waves in a 2D periodic multistable network. Loaded by a point force on the left, a transition front propagates through the structure, transforming unit cells from an open (strained) to a closed (unstrained) state as the domain wall passes by. Lattice defects and boundaries can be used effectively to predicatively guide the wave in the laser-cut polymer sheet (the right boundary acts as a rigid wall here).

Movie S2. 1D transition wave

Experimental realization of a 1D transition wave in a long multistable chain compared with numerical result from the continuum model. Upon initiation from the left, a 1D transition wave travels through the structure.

Movie S3. 2D transition wave

Experimental observations of transition waves propagating through 2D structures (after initialization in the fully open configuration, each transition wave is triggered by a point load applied by the black indenter). Waves are controlled by boundary conditions (e.g., boundary application sites) as well as by defects (e.g., point defects realized by non-transforming open unit cells). Examples show free transition wave propagation in two directions, wave pinning, wave deflection and rotation. Numerical results obtained from the continuum model are in good qualitative agreement with experimental findings, with differences stemming mainly from imperfections and size effects.

Movie S4. Transition waves in complex structures

The continuum model is used to explore and expand the design space and realize transition waves in various reconfigurable complex systems,as demonstrated by the following simulated examples:

First, by combining the effects of point defects and free surfaces, a transition front is designed to produce a serpentine motion suitable e.g. locomotion of soft robots.

Second, combining point defects with complex shapes having interior and exterior surfaces adds functionality such as splitting and merging of waves, resulting in morphing devices as demonstrated in a reconfigurable body.

Third, a hollow tube made of a multistable sheet with four different unit cell geometries in five sections (each producing a distinct energy landscape) results in a structure in which the transition wave adjusts its speed in each section. The color map shows the relative change in unit cell area.

Movie S5. Transition wave in a large 2D sample

Propagation of transition wave in a large 2D sample showing a curved front.

References

1. M Senn, C Eberl, Digital image correlation and tracking. *[Computer Software] https://uk. mathworks. com/matlabcentral/fileexchange/50994-digital-image-correlation-andtracking* (2015).
2. N Nadkarni, C Daraio, R Abeyaratne, DM Kochmann, Universal energy transport law for dissipative and diffusive phase transitions. *Phys. Rev. B* **93**, 104109 (2016).
3. J Qiu, JH Lang, AH Slocum, A curved-beam bistable mechanism. *J. microelectromechanical systems* **13**, 137–146 (2004).